2015

# Electrolyte pore/solution partitioning by expanded grand canonical ensemble Monte Carlo simulation

F. Moucka

D. Bratko
*Virginia Commonwealth University*, dbratko@vcu.edu

A. Luzar

# Electrolyte pore/solution partitioning by expanded grand canonical ensemble Monte Carlo simulation

Filip Moucka,[1,2] Dusan Bratko,[1,a)] and Alenka Luzar[1,b)]
[1]*Department of Chemistry, Virginia Commonwealth University, Richmond, Virginia 23221, USA*
[2]*Faculty of Science, J. E. Purkinje University, 400 96 Ústí nad Labem, Czech Republic*

(Received 3 January 2015; accepted 23 February 2015; published online 27 March 2015)

Using a newly developed grand canonical Monte Carlo approach based on fractional exchanges of dissolved ions *and* water molecules, we studied equilibrium partitioning of both components between laterally extended apolar confinements and surrounding electrolyte solution. Accurate calculations of the Hamiltonian and tensorial pressure components at anisotropic conditions in the pore required the development of a novel algorithm for a self-consistent correction of nonelectrostatic cut-off effects. At pore widths above the *kinetic* threshold to capillary evaporation, the molality of the salt inside the confinement grows in parallel with that of the bulk phase, but presents a nonuniform width-dependence, being depleted at some and elevated at other separations. The presence of the salt enhances the layered structure in the slit and lengthens the range of inter-wall pressure exerted by the metastable liquid. Solvation pressure becomes increasingly repulsive with growing salt molality in the surrounding bath. Depending on the sign of the excess molality in the pore, the wetting free energy of pore walls is either increased or decreased by the presence of the salt. Because of simultaneous rise in the solution surface tension, which increases the free-energy cost of vapor nucleation, the rise in the apparent hydrophobicity of the walls has not been shown to enhance the volatility of the metastable liquid in the pores. © *2015 AIP Publishing LLC.* [http://dx.doi.org/10.1063/1.4914461]

## I. INTRODUCTION

The advent of highly porous materials, from organometallic networks[1] to graphitic foams[2] and composites,[3] is giving rise to renewed interest in fluid adsorption in nanoporous substances. Pore permeation by electrolytes is important in a diverse range of applications, from heterogeneous catalysis to energy storage to separation techniques. Nanoconfined liquids feature significant differences from their macroscopic counterparts.[4] Predicting the composition of confined solutions requires the understanding of the equilibrium with the surrounding bath, which determines solvent and solute chemical potentials. Such understanding can be gained primarily from studies at the molecular level. Molecular modeling represents a powerful tool in characterization of nano-confined solutions. Grand Canonical Monte Carlo (GCMC) simulations,[5–7] which bypass costly computations of the bulk phase, have traditionally represented the method of choice in studies of adsorption equilibria in aqueous systems. Phenomena of interest include pore condensation (from gaseous surrounding) or evaporation,[8,9] infiltration from and expulsion to the liquid bath,[10–13] and composition changes in mixtures with selective component affinities to nanopore material.[14,15] The propensity for ion adsorption depends on charge and permittivity of confining walls, packing effects, and the extent of ion hydration in narrow confinements.[16,17] The interplay of these effects has been considered in a number of Molecular Dynamics (MD) simulations.[17–21] Quasi-grand canonical systems used in MD simulations are restricted to confinements of finite lateral dimensions, placed in a reservoir with a sizeable bulk-like region to maintain essentially unperturbed chemical potentials of solution components. Long equilibration and sampling times are typically necessary to capture constant chemical potential situations by this technique. The use of open ensemble Monte Carlo (MC) methods and particle insertion techniques in the presence of ions, on the other hand, has typically been limited to implicit solvent models.[20,22–30] Huge free energy changes associated with insertions or removals of ions (several hundred $kT$ for monovalent salts at ambient conditions) result in prohibitively small exchange acceptances for ion pairs in aqueous solutions (represented by either of conventional molecular models) at ambient conditions.[31,32] Recent studies of bulk electrolytes showed the problem can be overcome by replacing one-step ion exchange attempts with sequences of incremental increases or decreases of ion coupling with the environment.[33–36] According to the expanded ensemble Monte Carlo[37] underlying these works, the fractional coupling for selected ion particles represents an additional degree of freedom varying between zero for completely decoupled particles and unity for a fully coupled ion pair. Subdividing this interval to around 20 partially decoupled states has been shown to secure finite transition acceptances and viable rate of ion exchanges. Notwithstanding the biased distribution[37] of partially charged states, the method satisfies grand canonical statistics in fully charged states, which are used in calculations of structural and thermodynamic properties of the solution. In a combination with the osmotic ensemble sampling, whereby the

a)Email: dbratko@vcu.edu
b)Email: aluzar@vcu.edu

 

fluctuations in the volume replace transfers of water molecules, the fractional ion approach allowed precise calculations of chemical potentials and ultimately salt solubilities in a series of model electrolyte systems.[33–36]

The present article describes an adaptation of the expanded ensemble Monte Carlo to study the behavior of nanoconfined salt solutions in equilibrium with (implicit) bulk phase, characterized by fixed water and electrolyte chemical potentials. We demonstrate the use of fractional GCMC changes for both the ions and water molecules to present a computationally viable sampling technique for confined electrolytes. A novel algorithm is introduced to replace the conventional tail correction associated with the truncation of noncoulombic interactions in a strongly anisotropic system. The application of the above methods is illustrated in the case of NaCl solutions in laterally extended nanopores of planar geometry (Fig. 1). We consider apolar confinements of widths slightly *above* the kinetic threshold for capillary evaporation of water,[11,12,38–40] which persists in the pores in a metastable liquid state.[11,41,42] Earlier studies suggested the addition of salt to render the solid/solution interface more hydrophobic,[18,43] raising the question of possible destabilization of the confined solution with respect to capillary evaporation.[20] We determine the amounts and interfacial distributions of confined water and salt ions for different concentrations of bulk solution. Well-defined charge layering, observed across entire pore, significantly extends the range of interfacial perturbations in the presence of the salt. To examine the effect of added electrolyte on wall wettability and associated solvation force, we estimate the changes in the solvation pressure acting on, and wetting free energies of, confining walls as functions of salt concentration in the *bath*. Our results reveal a non-monotonic variation of excess salt molality and wetting free energy on the width of the confining slit, which persists even at several nm inter-wall separations. The observed interplay between molecular packing effects and Coulombic and dispersion interactions highlights the importance of all-atom simulation techniques for studies of nanoconfined electrolytes. The approach we describe in Sec. II overcomes major hurdles that have been impeding the use of Monte Carlo techniques in these complex systems. In Sec. III, we present the results for main structural and thermodynamic properties of our prototypical model systems. We discuss these results in the context of earlier studies of related systems, which were primarily based on molecular dynamics simulations.[17–20,44,45] Section IV summarizes main findings and briefly discusses the perspectives of Monte Carlo approaches for studies of electrolytes in nanoparticle dispersions, inside porous materials, or at submerged surface corrugations in contact with unperturbed salt solution.

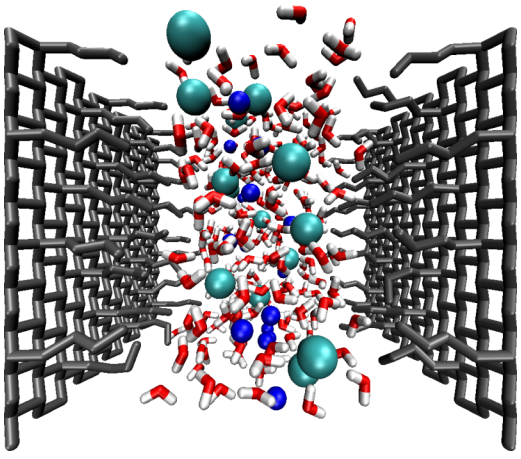

FIG. 1. A snapshot of the simulation cell with electrolyte solution between a pair of hydrophobic plates. The system is periodically replicated in lateral directions and maintains equilibrium with an (implicit) reservoir at ambient conditions and fixed concentration of the salt.

## II. METHODOLOGY

### A. Models

We model water using the standard SPC/E force field.[46] For NaCl, we use the model of Joung and Cheatham[47,48] (JC). This model has been shown to produce reasonable results for aqueous NaCl solutions at ambient conditions.[34–36,48,49]

The interactions between all types of particles in solution are modeled by a sum of Lennard-Jones (LJ) interactions,

$$U_{ij,LJ} = 4\varepsilon_{ij}\left[\left(\frac{\sigma_{ij}}{r_{ij}}\right)^{12} - \left(\frac{\sigma_{ij}}{r_{ij}}\right)^{6}\right] \tag{1}$$

and Coulombic interactions,

$$U_{ij,\mathrm{Coul}} = \frac{q_i q_j}{4\pi\varepsilon_0 r_{ij}}, \tag{2}$$

where $\varepsilon_{ij}$ and $\sigma_{ij}$ are, respectively, the LJ well-depth and LJ size parameters, $r_{ij}$ is the distance between the interacting sites $i$ and $j$, $q_k$ is the charge at the center of the interacting site $k$, and $\varepsilon_o$ is the permittivity of vacuum. The models embody a single LJ site that either coincides with the center of the oxygen atom (O) for the water or the ion centers. We use the Lorentz-Berthelot combining rules[5] for the cross LJ parameters,

$$\varepsilon_{ij} = \sqrt{\varepsilon_{ii}\varepsilon_{jj}}, \qquad \sigma_{ij} = \frac{\sigma_{ii} + \sigma_{jj}}{2}. \tag{3}$$

For the values of Lennard-Jones parameters, we refer the reader to the original papers.[46–48]

We model interactions between the particles and walls of the pore by two approaches. The first model considers smooth walls (SW) represented by the integrated (9-3) Lennard-Jones particle-wall potential[7,11,12,14,15,50–52]

$$U_{i,\,\mathrm{SW}} = A_i\left(\frac{\sigma_{i\mathrm{w}}}{r_{i\mathrm{w}_1}}\right)^9 - B_i\left(\frac{\sigma_{i\mathrm{w}}}{r_{i\mathrm{w}_1}}\right)^3 + A_i\left(\frac{\sigma_{i\mathrm{w}}}{r_{i\mathrm{w}_2}}\right)^9 - B_i\left(\frac{\sigma_{i\mathrm{w}}}{r_{i\mathrm{w}_2}}\right)^3, \tag{4}$$

where $r_{i\mathrm{w}_1}$ and $r_{i\mathrm{w}_2}$ are the distances of particle $i$ from the two walls in the planar pore, $A_i = 4/45\pi\rho_{\mathrm{w}}{\sigma_{i\mathrm{w}}}^3\varepsilon_{\mathrm{iw}}$, $B_i = 15/2\ A_i$, $\rho_{\mathrm{w}}$ is the presumed uniform number density of interacting sites of wall material, $\sigma_{i\mathrm{w}}$ and $\varepsilon_{\mathrm{iw}}$ are obtained by the Lorentz-Berthelot rules and LJ parameters of the wall interaction sites, $\sigma_{\mathrm{w}}$ and $\varepsilon_{\mathrm{w}}$. To mimic hydrocarbon walls, we use $\rho_{\mathrm{w}} = 0.0333$ Å$^{-3}$, $\varepsilon_{\mathrm{w}} = 0.6483$ kJ mol$^{-1}$, $\sigma_{\mathrm{w}} = 3.742$ Å.

The second model considers walls with discrete interaction sites representing butylated graphane surfaces,[53] hereafter called molecular walls (MW). These nonpolarizable surfaces have similar wetting properties as self-assembled monolayer (SAM)-coated substrates but possess a considerably simpler

structure advantageous in computational setting.[21,53,54] The structure of the MW was prepared by a molecular dynamics simulation using a flexible model in united-atom representation[55] and then transformed to a rigid structure as detailed in previous works.[44,53,56] Interactions of the MW with the solution are of Lennard-Jones type.[44,53,56] Parameters of interaction sites representing united-atom groups adopted from Jorgensen *et al.*[55] had the following values: $\sigma_{CH3} = 3.905$ Å, $\sigma_{CH2} = 3.905$ Å, $\varepsilon_{CH2} = 0.7866$ kJ mol$^{-1}$, $\sigma_{CH} = 3.85$ Å, $\varepsilon_{CH} = 0.3347$ kJ mol$^{-1}$, $\sigma_C = 3.8$ Å, $\varepsilon_C = 0.2092$ kJ mol$^{-1}$. For comparison with strongly hydrophobic systems previously studied in neat water,[11,12,52,57] we adjust $\varepsilon_{CH3}$ to 0.3347 kJ mol$^{-1}$ corresponding to contact angle ~130° ± 2°.

### B. Methods

We simulate the solution confined between two infinite parallel walls by a MC method based on grand canonical approach.[58] The solution in the nanopore is in equilibrium with an implicit bulk reservoir (not simulated) with temperature $T$ = 298 K, pressure $P \sim 1$ bar, and molality $m_{bulk} \leq 6$ mol kg$^{-1}$. Chemical potentials in the nanopore, $\{\mu_i\}$, $i = 1 \ldots t$, where $t$ is the number of species in the solution, are equal to those in the reservoir. Chemical potentials, therefore, represent input parameters for the simulation of the solution in the nanopore. Chemical potential values are available in recent literature[36] in the form of analytic functions of concentration for the NaCl aqueous solution modeled by the SPC/E and JC force fields at ambient conditions. These functions are, therefore, readily used in the present work for the chemical potentials of NaCl and of water,

$$\mu_{NaCl} = \mu^{\dagger}_{NaCl} + 2RT \ln m + 2RT \ln(10) \times \left(-\frac{A\sqrt{m}}{1 + B\sqrt{m}} + bm + Cm^2 + Dm^3\right), \quad (5)$$

$$\mu_{H_2O} = \mu^{*}_{H_2O} - 2RTmM_{H_2O} - RTM_{H_2O}\ln(10) \times \left(bm^2 + \frac{4}{3}Cm^3 + \frac{3}{2}Dm^4 + \frac{2A}{B^3 + B^4\sqrt{m}} + \frac{4A\ln(B\sqrt{m}+1)}{B^3} - \frac{2A\sqrt{m}}{B^2} - \frac{2A}{B^3}\right), \quad (6)$$

where $A = 0.5108$, $B = 1.4495$, $\mu^{\dagger}_{NaCl} = -391.278$ kJ mol$^{-1}$, $\mu^{*}_{H_2O} = -240.301$ kJ mol$^{-1}$, $b = 0.019\,088$, $C = 0.021\,530\,7$, $D = -0.001\,335\,6$, and $m$ stands for the reduced electrolyte molality ($m_{bulk}$/mol kg$^{-1}$).

### C. Implementation of the grand canonical Monte Carlo method

During the simulation, a sequence of configurations is generated as in the case of a constant numbers of particles, volume, temperature (*NVT*) MC simulation, with an additional MC step (for each independent species) changing the numbers of particles $\{N_i\}$ by $\{\Delta N_i\}$, $i = 1 \ldots t$. Acceptance probability criterion that governs this MC step[34] is

$$\Pi(\{N_i\} \rightarrow \{N_i + \Delta N_i\}) = \min\{1; [\Pi_{i=1}^{t} \frac{N_i!}{(N_i + \Delta N_i)!}(V\beta P^0)^{\Delta N_i}]e^{(-\beta(\Delta U + \Delta G^p))}\}, \quad (7)$$

where $V$ is the volume in which new particles are created or deleted (it should roughly match the interior of the nanopore available to the particles for a good efficiency), $\beta = 1/k_BT$, $k_B$ is the Boltzmann constant, $P^0$ is the standard-state pressure (1 bar), $\Delta U$ is the configurational energy change of the MC step, and

$$\Delta G^p = -\sum_{i=1}^{s}(\mu_i - \mu_i^0)\Delta N_i \quad (8)$$

is an externally prescribed free energy driving force (at fixed pressure $p$), where $\mu_i$ and $\mu_i^0$ are, respectively, the total chemical potential and the ideal-gas standard chemical potential per particle of species $i$. Values of the ideal-gas standard chemical potentials, $\mu_i^0$, are available in thermochemical compilations such as the NIST-JANAF,[59] Thermodynamics Research Center,[60] or Wagman tables.[61] We use $\mu_w^0 = -228.582$ kJ mol$^{-1}$, $\mu^0_{Na^+} = 574.317$ kJ mol$^{-1}$, $\mu^0_{Cl^-} = -240.167$ kJ mol$^{-1}$.[59]

The acceptance probability for direct GCMC insertion/deletion of ionic species in an aqueous solution via a single MC step, determined by Eq. (7), is, however, virtually zero due to the huge free energy change associated with the process. To overcome this difficulty, we utilize a method previously used for MC simulations of univalent salts in an osmotic ensemble.[34–36] The method is based on gradual insertion/deletion of the particles via a sequence of values of a coupling parameter, $\lambda_j$, corresponding to intermediate states (or fractional particles). We break a general process of changing particle counts

$$\text{initial state} \overset{\Delta G^P}{\Longleftrightarrow} \text{final state} \quad (9)$$

into sub-processes, which represent transitions between neighboring $\lambda$-states corresponding to fractional particles (frac. part.), i.e.,

$$\text{initial state}(\lambda_0 = 0) \overset{\Delta G_0^P}{\Longleftrightarrow} \text{fract. part.}(\lambda_1) \overset{\Delta G_1^P}{\Longleftrightarrow} \text{fract. part.}(\lambda_2) \ldots \overset{\Delta G_{M+1}^P}{\Longleftrightarrow} \text{final state}(\lambda_{M+2} = 1), \quad (10)$$

where

$$\Delta G^p = \sum_{j=0}^{M+1} \Delta G_j^p. \quad (11)$$

The first subprocess changing $\lambda_0$ to $\lambda_1$ represents insertion of new noninteracting particles. During the following steps, the value of $\lambda$ is gradually increased and the coupling of the fractional particles to the system becomes stronger. More specifically, the interactions of the fractional particles are dependent on the value of $\lambda$ via a conveniently devised scaling scheme as discussed further along Eqs. (14), (15), and (16). When $\lambda_{M+2}$ state is achieved, the fractional particles are fully interacting. These subprocesses can be understood as virtual chemical reactions turning existing fractional particles to new fractional particles with different values of $\lambda$. These intermediate steps are governed by Eq. (7) where $\{N_i\}$ correspond to the numbers of intermediate species and $\{\Delta N_i\}$ are their changes due to the reactions. For example, in the case of inserting a new noninteracting molecule, Eq. (7) becomes

$$\Pi_0 = \min\{1; V\beta P^0 e^{-\beta\Delta G_0^p}\} \quad (12)$$

and for increasing the $\lambda$ value of the molecule by the following steps of Eq. (10),

$$\Pi_j = \min\{1; e^{-\beta(\Delta U + \Delta G_j^{\mathrm{p}})}\}, \tag{13}$$

where the choice of the $\Delta G_j{}^{\mathrm{p}}$ values is explained later in this section and given by Eq. (17).

In the case of GCMC simulation of NaCl aqueous solution, we consider two processes changing particle counts, corresponding to two instances of Eq. (9). One process changes the amount of water in the nanopore. The other process changes the amount of $Na^+$ and $Cl^-$ ions simultaneously, thus maintaining electric neutrality of the solution. The acceptance probability criteria governing individual subprocesses are readily derived from Eq. (7), therefore these equations are not shown. In a simulation, each of the two processes is selected with equal probability 0.5, and its direction is also selected with equal probability 0.5. This ensures that the microscopic reversibility condition is satisfied. We only allow one such process to take place at a time, i.e., no new process is started when another process is still running, and only configurations with no intermediate particles are used for the averaging of thermodynamic and structural properties of the solution.

Regarding the scaling scheme, we employ equidistantly distributed values of $\lambda$, i.e., $\lambda_{j+1} = \lambda_j + \Delta\lambda$, and the two following approaches[34] are applied simultaneously: (i) scale all the site-site interaction potentials by a coupling parameter $\lambda$, which is the product of the individual coupling parameters $\lambda(i)$ and $\lambda(j)$ of the interacting molecules $i$ and $j$, i.e., $\lambda = \lambda(i)\lambda(j)$, and (ii) add a term of the form $[R_s\ (1-\lambda)]^2$ to the squared distance between the interacting sites, $r^2$. The scaled site-site interaction potential then becomes

$$u(r,\lambda) = \lambda u(r^*), \tag{14}$$

where

$$r^* = \{r^2 + [R_s(1-\lambda)]^2\}^{\frac{1}{2}} \tag{15}$$

and $u$ is a general site-site potential of any form. $R_s$ is an *ad hoc* parameter comparable to molecular size. This scheme is applied both to interactions within the solution and to solution-wall interactions in the case of molecular walls. In the case of interactions of particles with smooth walls, approach (i) is applied in the same way, i.e., Eq. (14) is applied to Eq. (4), where $u(r^*)$ represents the particle-wall potential, however, a slightly modified formula

$$r^* = r + R_s(1-\lambda) \tag{16}$$

is used in rescaling the particle-wall distance. The parameter $R_s$ in Eq. (15) is adjusted to achieve roughly evenly distributed acceptance ratios for all intermediate $\lambda$-states. Empirically, we find it optimal to split the process of inserting or deleting a water molecule to 5 subprocesses of different $\lambda$ values and the process changing the amount of NaCl to 15 such subprocesses, and we use $R_s = 2.5$ Å.

We set the $\Delta G_j{}^{\mathrm{p}}$ according to

$$\Delta G_j^{\mathrm{p}} = w_{j+1} - w_j + (\lambda_{j+1} - \lambda_j)\Delta G^{\mathrm{p}};$$
$$j = 0, 1, \ldots, M+1, \tag{17}$$

where $w_j$ are biasing weights assigned to the intermediate $\lambda$-states, and $w_0 = w_{M+2}$. The biasing weights $w_j$ are adjusted during the equilibration phase of the simulation by an iterative Wang-Landau (WL)[62] procedure, which ensures that the relative occurrences of all $\lambda$-states are roughly equal during the simulation.[34,37]

All values of $w_j$ are initially set to zero, $w_j{}^0 = 0$. During the equilibration period, when the system visits state $\lambda_j$, the corresponding value of $w_j$ is adjusted according to

$$w_j = w_j^0 + \Delta w. \tag{18}$$

The parameter $\Delta w$ is initially set to a value that provides reasonable convergence of the histograms of the $\lambda$-states during the first iteration. The histograms are then collected, and when the relative occurrences of all $\lambda$-states become reasonably high, the histograms are zeroed, $\Delta w$ is divided by two, and the process repeated. The iterations are stopped when $\Delta w$ meets a specified lower threshold. In addition, after each WL iteration, a constant is added to all values of $w_j$ to set their average to zero. This prevents numerical overflow of the $w_j$-values without affecting the relative occurrence of the $\lambda$-states. Here, we use the initial value of $\Delta w = 5 \times 10^{-23}$ J, we decrease $\Delta w$ and zero the accumulators when the relative occurrence of each $\lambda$-state becomes greater than 0.7, and the iteration is stopped when $\Delta w$ drops below $10^{-26}$ J. As this iteration takes place in a relatively short part of the simulation, the choice of the numerical values of these parameters is of marginal importance provided that the values of $w_j$ converge. Our choice is based on experience from previous simulations[34] in bulk solutions.

### D. Treatment of the long range electrostatic interactions and the Lennard-Jones tail corrections

As the simulated system is inhomogeneous, the standard isotropic tail correction to LJ interactions, i.e., based on the assumption $g(r) \approx 1$ for $r > r_c$, is not applicable. Special methods thus have to be used. Here, we use a method based on considerations similar to those introduced by Janecek[63] and later simplified by Blas *et al.*[64] We apply a cylindrical cut-off, i.e., we consider the total energy of the system due to the LJ interactions expressed by

$$U_{\mathrm{LJ}} = \frac{1}{2}\sum_{i=1}^{N}\Big(\sum_{j\in R_c^{(i)}} u(r_{ij}) + U_i^{\mathrm{LRC}}\Big), \tag{19}$$

where the notation means that the second sum runs over all particles $j$ located inside the cylinder of radius $R_c$ with its axis perpendicular to the planar pore and centered at the position of particle $i$. $U_i^{\mathrm{LRC}}$ (LRC stands for long range correction) represents the energy of intermolecular interactions between particle $i$ and all particles outside the cylinder. The Lennard-Jones interactions of particle $i$ with particles inside the cylinder are calculated directly by Eq. (1) subject to Eqs. (14) and (15) in the case of fractional particles. The interaction with particles outside the cylinder is approximated by an interaction with a continuum whose number density is homogeneous in the directions parallel to the pore. The number density of each species $k$ of the solution outside the cylinder is, therefore, considered to be a function of only $z$, i.e., $\rho_k = \rho_k(z)$, where $z$ is the

coordinate on the axis perpendicular to the pore. Furthermore, $\rho_k(z)$ is considered to be equal to the corresponding number density $\rho_k{}^{\text{in}}(z)$ measured inside the simulation box. $\rho_k{}^{\text{in}}(z)$, therefore, assumes the form of the Dirac δ function, which is infinite at each $z$ at which a particle is found in the simulation cell and zero elsewhere. The spatial distribution of the number density outside the central box, therefore, corresponds to a set of infinite planes parallel to the pore and of given surface number density, with a plane $j$ found for each particle $j$ in the simulation box at the same position, $z_j$. Fig. 2 depicts a typical situation where particle $j$ is outside the cylinder and its corresponding plane $j$ is represented by the light grey color. The surface number density of each of these planes is $1/S$ where $S = L_x L_y$ is the lateral area of the simulation cell. Consequently,

$$U_i^{LRC} = \sum_{j=1}^{N} u^{LRC}(z_{ij}), \tag{20}$$

where $u^{\text{LRC}}(z_{ij})$ is the interaction energy of particle $i$ with the part of the plane $j$ outside the cylinder and $z_{ij} \equiv |z_i - z_j|$. $u^{\text{LRC}}(z_{ij})$ is obtained by integrating energetic contributions with individual surface elements, $\mathrm{d}S = 2\pi R \mathrm{d}R$, of this plane represented by the dark grey circle in Fig. 2, where the integration runs over the distance from the axis of the cylinder, $R$, from $R_c$ to ∞,

$$u^{LRC}(z_{ij}) = \frac{2\pi}{S} \int_{R_C}^{\infty} R dR\, u_{ij}\left(\sqrt{R^2 + z_{ij}^2}\right). \tag{21}$$

In the specific case of LJ potential,

$$u^{LRC}(z_{ij}) = \frac{4\pi\varepsilon_{ij}}{S}\left(\frac{\sigma_{ij}^{12}}{5(R_c^2 + z_{ij}^2)^5} - \frac{\sigma_{ij}^{6}}{2(R_c^2 + z_{ij}^2)^2}\right). \tag{22}$$

Thus, $U_{\text{LJ}}$ is conveniently calculated as a sum of pair interactions and 1/2 of a sum of interactions of all particles with their own planes,

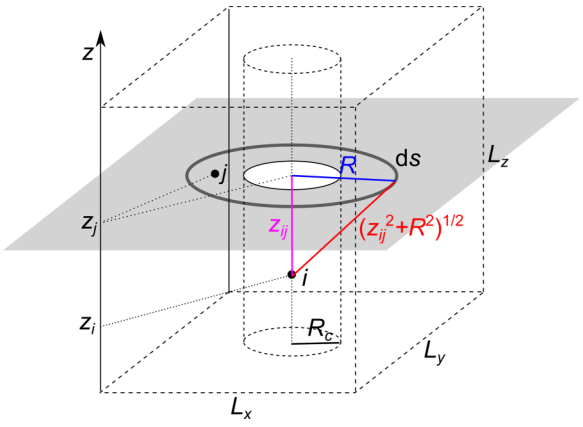


FIG. 2. The design for the tail correction of the cylindrical cut-off of non-coulombic interactions. The contribution of atoms at vertical distance $z_{ij}$ and radial distance exceeding the cylindrical cut-off plane $r_{xy} > R_c$ from the particle under consideration is approximated by a uniform area density $1/L_xL_y$ located at vertical distance $z_{ij}$ and integrated over all radial distances $r_{xy} > R_c$.

$$U_{LJ} = \sum_{i=1}^{N-1} \sum_{j=i+1}^{N} \left(u_c(r_{ij}) + u^{LRC}(z_{ij})\right) + \frac{1}{2}\sum_{i=1}^{N} u^{LRC}(0), \tag{23}$$

where $u_c(r_{ij}) = u(r_{ij})$ when particle $j$ is within the cut-off cylinder of particle $i$ and $u_c(r_{ij}) = 0$ when it is outside the cut-off cylinder. Analogous approach can be readily incorporated into any simulation program for anisotropic systems as it introduces only a changed pair-additive potential and a correction, independent on the positions of particles. We use $R_c = 9.8$ Å, which is close to our preceding studies of the bulk electrolytes[34] and aqueous confinements.[52,65]

We treat long-ranged electrostatic interactions by the standard Ewald summation method augmented by the Yeh-Berkowitz correction[66] for systems periodic only in lateral dimensions. We use the value of the screening parameter $\alpha = \pi/R_c$ and $15 \times 15 \times 19$ vectors in the reciprocal space. Nineteen vectors are used in the direction perpendicular to the pore in which a distance of 10 nm separates the individual periodic images of the pore.

The additional energy contributions discussed above are scaled according to Eqs. (14) and (15). Specifically, $u^{\text{LRC}}(z_{ij})$ is multiplied by $\lambda(i)\lambda(j)$ for interactions involving fractional particles, and $q_i$ is multiplied by $\lambda(i)$ for the calculation of the Fourier-space contribution of fractional particle $i$. Comparisons between our results for pure water with or without tail corrections show minor differences between the two approaches provided we use chemical potentials predetermined at the level of approximation identical to the one used in the confinement. The use of tail corrections is critical for electrolyte solutions since available chemical potentials correspond to bulk systems treated *with* long-range corrections for LJ interactions.[34–36]

### E. Pressure tensor components and wetting free energy calculation

Simulated averages of pressure tensor components in the direction perpendicular to the pore, $\langle P_\perp \rangle = \langle P_{zz} \rangle$, and lateral to pore walls, $\langle P_\parallel \rangle \approx \langle P_{xx} \rangle \approx \langle P_{yy} \rangle$, are estimated numerically following earlier works[16,51,67,68]

$$\begin{aligned}\langle P_\perp \rangle &= \frac{1}{\beta L_{xy}^2 L_z}\left[\langle N \rangle + \frac{1}{2\delta_z} \ln\langle e^{-\beta \Delta U(L_z(1-\delta_z)\to L_z(1+\delta_z))}\rangle\right], \\ \langle P_\parallel \rangle &= \frac{1}{\beta L_{xy}^2 L_z} \\ &\quad \times \left[\langle N \rangle + \frac{1}{4\delta_{xy}} \ln\langle e^{-\beta \Delta U(L_{xy}(1-\delta_{xy})\to L_{xy}(1+\delta_{xy}))}\rangle\right].\end{aligned} \tag{24}$$

Equation (24) implies the equality $\langle P_\parallel \rangle = \langle P_{xx} + P_{yy} \rangle/2$, consistent with the symmetry of the system. $\langle N \rangle$ is the average number of particles in the simulation cell of base area $L_{xy}{}^2$ and height $L_z$, $\Delta U$ is the potential energy change associated with scaling of cell dimensions and molecular coordinates by the scaling factor $\alpha_z = 1 + \delta_z$ or $\alpha_{xy} = 1 + \delta_{xy}$. To verify the accuracy of the finite difference approximation[67] for the excess pressure components in Eq. (24), we used three values of $\delta$ parameters spanning the interval $10^{-6} < |\delta| < 10^{-4}$. Results obtained by using different $\delta$ parameters from the specified

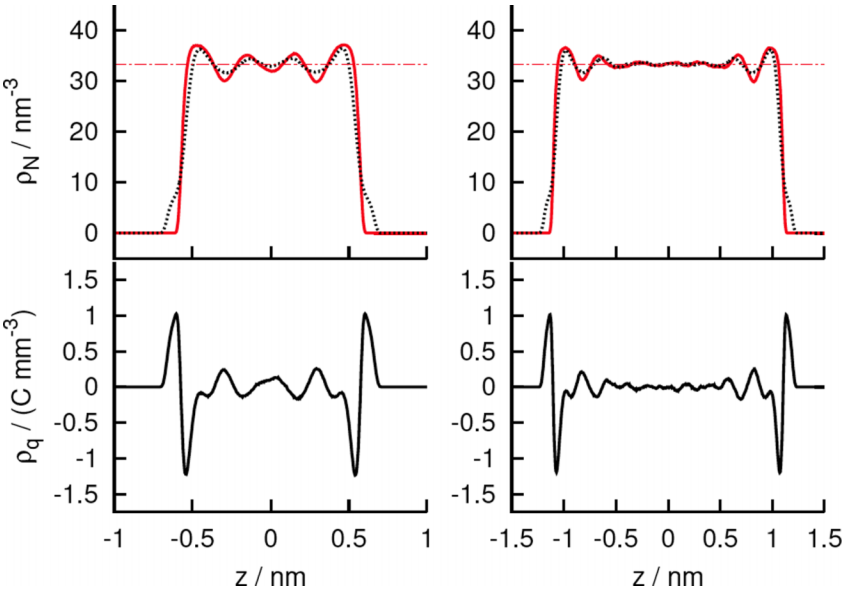


FIG. 3. Number density profiles $\rho_N$ of oxygen atoms (red solid lines), half the number density of hydrogen atoms (black dotted lines), and combined charge density $\rho_q$ due to partial charges on both atomic species (solid black) in pores of diameter $h = 1.64$ nm (left) or 2.7 nm (right). Horizontal lines denote number density values in the corresponding bulk reservoirs.

range mutually agree and their systematic errors due to the numerical estimates of the derivatives are much smaller than their statistical uncertainties due to the limited sampling of the configurational space.

To provide an additional test of the above approach, we also calculate $\langle P_{zz} \rangle$ directly from the net force per unit area of the wall. The force is calculated by *analytically* differentiating the total potential energy with respect to the $z$-position of the wall even in the case of the molecular wall model because the cylindrical cut-off and the long range corrections yield a smooth potential energy function of $z$-positions of all particles including the interaction sites constituting the wall. In all our simulations, the values of $P_{zz}$ calculated by Eq. (24) and by the direct calculation of forces mutually agreed within their statistical uncertainties.

The wetting free energy, defined as the change in grand potential $\Omega(\{\mu_i\}, h, T)$ per unit area ($A$) of wetted nanopore walls, $\sigma = (\partial\Omega/\partial A)_{\{\mu_i\},h,T}$, is calculated according to the relation $\sigma = -\langle P_{\parallel} \rangle h/2$, where $h$ is the thickness of the pore.[51] In contrast to macroscopic systems, in our nanosized pores, $h$

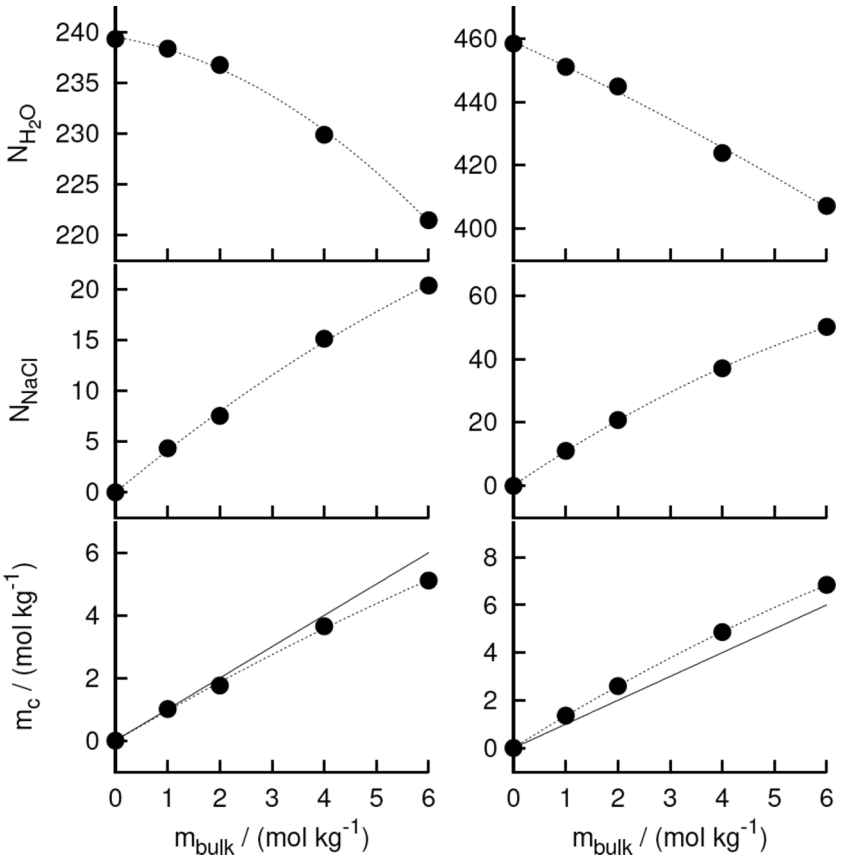


FIG. 4. Number of water molecules (1st row) and $Na^+Cl^-$ ion pairs (2nd row) in 1.64 nm (left) or 2.7 nm wide confinement (right) as a function of NaCl molality in the bulk phase. 3rd row: average molality inside the confinement, $m_c$, as function of bulk NaCl molality, $m_{bulk}$, at the two widths of the pore. Dotted lines are guide for the eye. Solid lines are bulk values. The size of the symbols denotes error bars.

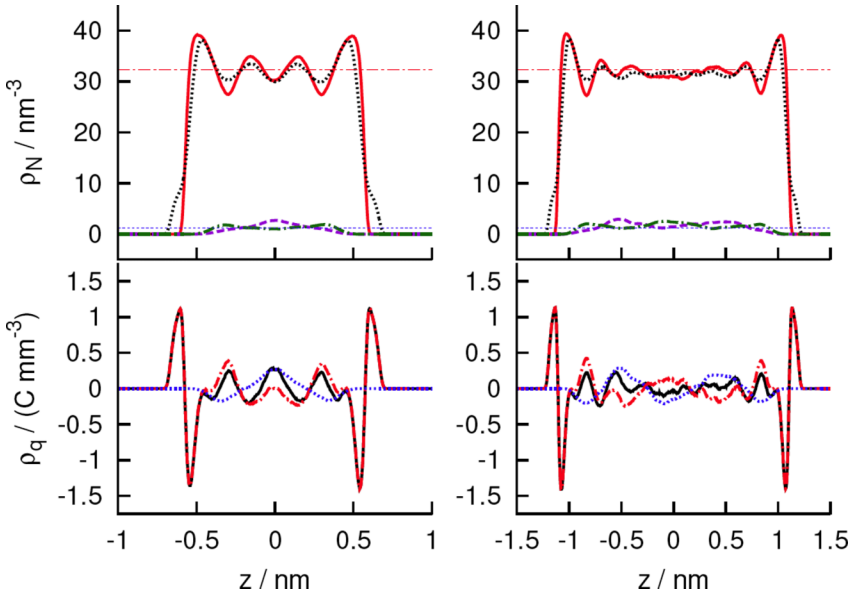


FIG. 5. Top: number density profiles of oxygen atoms (red, solid lines), half the number density of hydrogen atoms (black, dotted lines), chloride (green, dotted-dashed), and sodium (purple, dashed) ions in pores of diameter $h$ = 1.64 nm (left) or 2.7 nm (right) at bulk NaCl molality $m_{\text{bulk}} = 2$ mol kg$^{-1}$. Bottom: net charge density profile (black, solid) and charge densities due to water molecules (red, dotted-dashed), and salt ions (blue, dotted). Horizontal lines denote number density values of water (red) and of ions (blue) in the corresponding bulk reservoirs.

is comparable to the range of molecular interactions, leading to a detectable dependence of the wetting free energy on the width of the pores.

## III. RESULTS AND DISCUSSION

To isolate effects of added salt on structural and thermodynamic properties of confined solution, we consider model systems well characterized in the absence of ions.[11,12,15,51] We choose two confinement widths: $h$ = 1.64 nm or 2.7 nm. For the selected wall hydrophobicity (contact angle around 130°), both separations are well inside the cavitation regime, with water persisting in the pore in metastable liquid state because of appreciable kinetic barrier to cavitation.[11,12,69] The narrower of the two pores features the smallest separation shown to consistently avoid evaporation at given hydrophobicity of the walls and timescales accessible in practical simulations. As illustrated in Fig. 3, when the narrower pore is filled with neat water, the layered water structure extends through the entire system. The bigger pore, on the other hand, is sufficiently wide to comprise two nearly independent interfacial layers separated by a region resembling bulk aqueous phase. The subtle differences in the density profiles of oxygen and hydrogen atoms reflect a bias in molecular orientations,[50,57,70] which varies with the distance from the wall.[43] As a result, local charge densities due to the partial charges on oxygen and hydrogen atoms are generally not cancelled, leading to notable oscillations in charge density within the first few solvation layers. These oscillations extend across entire pore at smaller diameter $h$ = 1.6 nm but become negligible around the midplane of the wider pore with $h$ = 2.7 nm.

Below, we examine if these properties change when the pore is in equilibrium with a reservoir of saline solutions. We use NaCl molalities ranging from 1 to 6 mol kg$^{-1}$. The upper molality limit is below NaCl solubility in bulk solution.[34,35] Apolar confinement walls with weak affinity for the ions do not

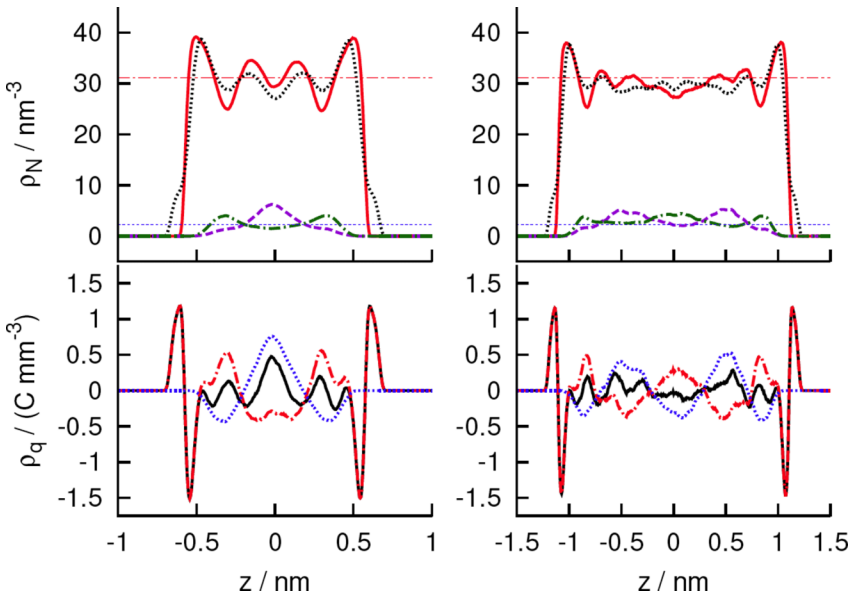


FIG. 6. Top: number density profiles of oxygen atoms (red, solid lines), half the number density of hydrogen atoms (black, dotted lines), chloride (green, dotted-dashed), and sodium (purple, dashed) ions in pores of diameter $h$ = 1.64 nm (left) or 2.7 nm (right) at bulk NaCl molality $m_{\text{bulk}} = 4$ mol kg$^{-1}$. Bottom: net charge density profile (black, solid) and charge densities due to water molecules (red, dotted-dashed), and salt ions (blue, dotted). Horizontal lines denote number density values of water (red) and of ions (blue) in the corresponding bulk reservoirs.

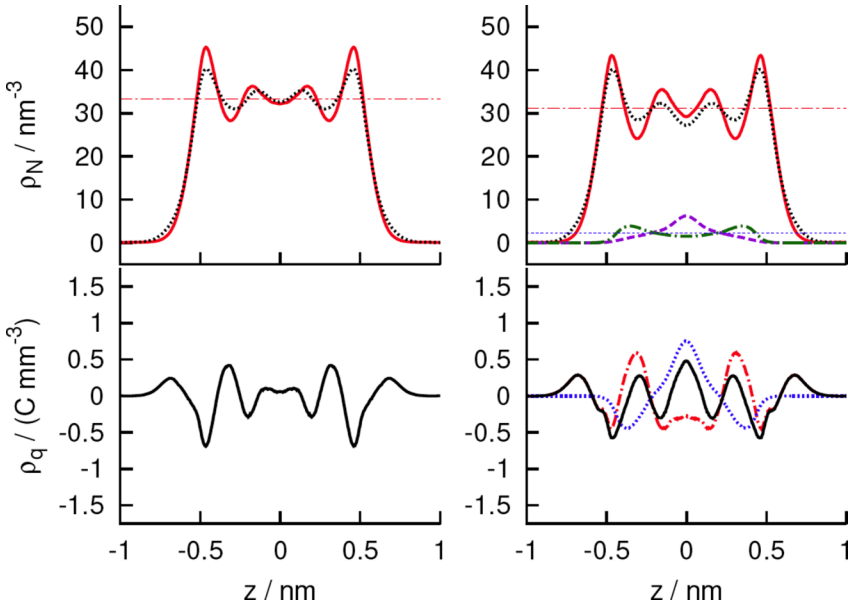


FIG. 7. Density profiles between parallel molecular walls at separation $h = 1.64$ nm in pure water (left) and bulk NaCl molality $m_{bulk} = 4$ mol kg$^{-1}$ (right). Top: number density of oxygen atoms (red, solid lines), half the number density of hydrogen atoms (black, dotted lines), chloride (green, dotted-dashed), and sodium (purple, dashed) ions. Bottom: total charge density (black, solid) and charge densities due to water molecules (red, dotted-dashed), and salt ions (blue, dotted). Horizontal lines denote number density values of water (red) and of ions (blue) in the corresponding bulk reservoirs.

assist crystal nucleation[71] and we observe no signs of precipitation even when the confinement molality exceeds that of the bulk phase. In the top two rows in Fig. 4, we show the numbers of water and NaCl molecules inside the periodically repeating confinement box with the area (2.5 nm)$^2$ and width 1.64 or 2.7 nm. While the share of NaCl ion pairs in the confinement increases with bulk concentration, the relative trends at the two pore widths are markedly different. As shown in the 3rd row of Fig. 4, the molality in the narrower confinement shows depletion, while we observe enhancement relative to the bulk value in the wider pore. Clearly, the molality inside the confinement converges to the bulk value at large widths. The nonmonotonic width dependence of the excess molality is explained in terms of the oscillatory ion distributions illustrated in Figs. 5 and 6 for $m_{NaCl} = 2$ mol kg$^{-1}$ and 4 mol kg$^{-1}$. These distributions follow the charge density layering in interfacial water, hence the packing efficiency of the ions is a nonmonotonic function of pore width. The overall molality in the pores is also reduced due to the exclusion of the ions from the first solvation layer (see Figs. 5-7), with net effect more significant in narrower pores. Apart from the differences due to the hydrophobic character of pore walls in the present study, essential structural features in the 1.64 nm pore conform to earlier MD results for confined NaCl carbon pores of similar (1.6 nm) width.[17]

The majority of our calculations employ smooth confinement walls with integrated (9-3) Lennard-Jones wall-water interaction mimicking hydrocarbon.[7,11,12,50,51] To verify if perfectly smooth walls exaggerate the structure in the interfacial layer, in Fig. 7, we present density profiles obtained with a more realistic model consisting of butylated graphane platelets, whose interface with water resembles a hydrocarbon SAMs surface.[53,56] The interfacial structures show little change upon replacement of smooth walls by a model with molecular resolution,[53] however, a somewhat enhanced layering of atomic densities and less pronounced polarization of surface water layer is observed in the latter case.

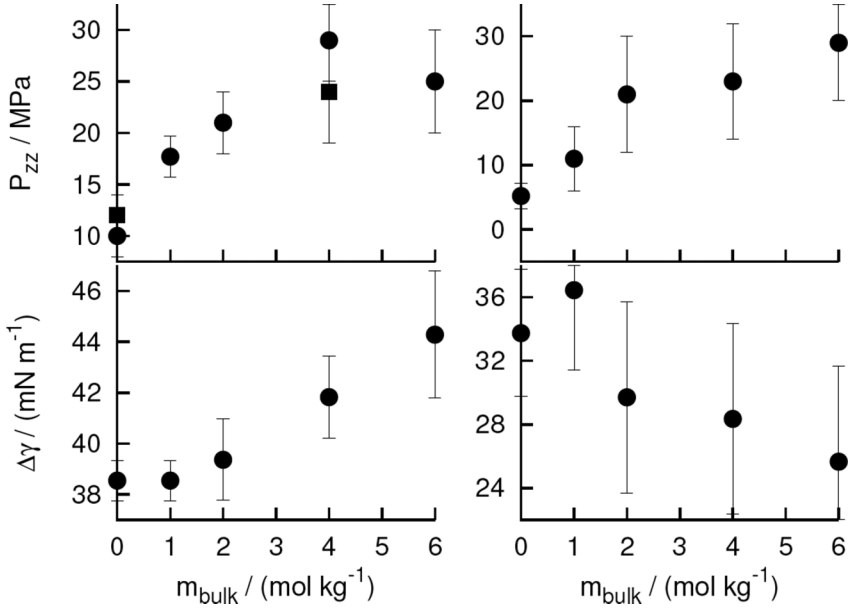


FIG. 8. Normal pressure acting on the confinement walls with intervening NaCl solution in metastable liquid state for two pore widths: $h = 1.64$ nm (left) or 2.7 nm (right) as a function of NaCl molality in the bulk phase (top). Wetting free energies of confinement walls $\Delta\gamma \equiv \sigma(h, m)$ as functions of bulk NaCl molality at the two widths of the pore (bottom). The symbols denote smooth wall (circles) and molecular wall (squares) systems.

Finally, we consider the changes of two thermodynamic properties, the mean of the normal component of the pressure tensor between confinement plates, $P_{zz}(h,m)$, and wetting free energy $\sigma(h,m)$, defined as the change of the confinement grand potential $\Omega(h,A,m)$ per unit area ($A$) of wetted walls. Note that, in the nanoconfinement, interfacial effects propagate throughout the entire volume; hence, the wetting free energy $\sigma$ sums up contributions from the whole pore rather than the surfaces alone. In Fig. 8, we show GCMC simulation results for both quantities, presented as functions of the bulk molality of NaCl. At both confinement widths we considered, the pressure shows a notable increase with salt molality in the bulk phase. While sampled pressures carry considerable numerical uncertainty, the overall trend is unambiguously showing the presence of salt to increase short-ranged repulsion, previously observed[11,42,72] between hydrophobic walls with neat intervening water in metastable liquid state. At the same time, salinity renders apolar walls more hydrophobic[20,43,45] and stabilizes the wall-wall contact configuration,[45,73] which corresponds to the globally stable state. The presence of salt leads to a wider gap between the metastable (liquid) and stable (cavitated) branches of free energy (grand potential $\Omega$) *vs.* distance ($h$) profiles.[42] The leading contribution to the difference between the two branches is free energy of wetting, $\sigma(h,m)$. In view of the above, $\sigma(h,m)$ is expected to increase with decreasing separation $h$ and the effect should be intensified by salinity. These trends are confirmed by comparing the dependence of $\sigma$ on $m_{NaCl}$ at two separations, $h$, shown in row 3 in Fig. 4. Specifically, the difference $\sigma(1.6\text{ nm}) - \sigma(2.7\text{ nm})$ is $4 \pm 2$ mN m$^{-1}$ in pure water and $19 \pm 2$ mN m$^{-1}$ at $m_{bulk} = 6$ mol kg$^{-1}$. In spite of the free energy increase of the (metastable) liquid phase in the confinement, simulations have not shown salinity to destabilize the liquid with respect to cavitation. Preserved metastability can be rationalized by concurrent increase in the nucleation barrier to cavitation due to the rise in liquid/vapor surface tension at increased salinity of confined solution.

## IV. CONCLUDING REMARKS

Nanopore wetting by salt solutions affects the performance of corrugated electrodes, the catalyst function in ionic reactions, decontamination of metal ions, dispersion stability, and ion-assisted biointeractions. Molecular modeling can provide helpful insights into these processes. However, because of huge energy changes upon addition or removal of ions, standard open-ensemble methodologies cannot be used to model adsorption processes of ions in GCMC simulations. We describe an extension of the fractional ion-exchange approach, previously applied in the osmotic ensemble for the bulk phase, to confined electrolyte systems subject to incremental, multistep exchanges of both the solvent *and* salt molecules. Through test calculations for NaCl solutions, we demonstrate that the method enables rigorous modeling of pore/bath equilibria without explicit inclusion of a bulk-like reservoir, which is typically necessary in molecular dynamics studies along with the use of laterally restricted pores.

Using fractional-exchange GCMC simulations in extended hydrophobic nanopores, we show that salt molality features a nonmonotonic dependence on pore width. Specifically, we observe salt depletion (compared to the bulk value) in narrow pores of width below 2 nm while molality is enhanced in about twice wider pores. The addition of the electrolyte does not promote capillary evaporation when confined water persists in a metastable liquid state. While the presence of electrolyte renders pore surfaces more hydrophobic,[43] increasing the *overall* attraction between the walls, the moderate-range solvation force in the metastable-liquid regime can actually acquire a repulsive contribution. In the narrower pores, the wetting free energy increases with bulk phase salinity, however, an opposite trend is detected in twice wider pores, consistent with salt depletion in the former, and (positive) adsorption in the latter case. Planned extensions of our GCMC approach will enable studies of combined effects of external electric field[51,52,57] and ion specificity[74] to facilitate tuning surface free energy, uptake of water and salt for potential use in capacitors, surface energy storage, nanofluidics, and electromechanical actuation. Generalizing the described methodology to the reaction ensemble Monte Carlo[75] will also allow us to address reaction equilibria in ionic solutions.

## ACKNOWLEDGMENTS

A.L. and D.B. acknowledge support from the U.S. Department of Energy, Office of Basic Science (DE-SC 0004406). F.M. thanks for support from Czech Science Foundation (Grant No. GP13-35793P). We also acknowledge supercomputing time allocations from the National Energy Research Scientific Computing Center (NERSC), supported by the Office of Science of the U.S. Department of Energy (DEAC02-05CH11231), and the Extreme Science and Engineering Discovery Environment (XSEDE), supported by NSF Grant No. OCI-1053575. Access to computing and storage facilities owned by parties and projects contributing to the National Grid Infrastructure MetaCentrum, provided under the programme "Projects of Large Infrastructure for Research, Development, and Innovations" (LM2010005), is greatly appreciated.

[1] J. Canivet, A. Fateeva, Y. M. Guo, B. Coasne, and D. Farrusseng, Chem. Soc. Rev. **43**, 5594 (2014).
[2] J. Biener, M. Stadermann, M. Suss, M. A. Worsley, M. M. Biener, K. A. Rose, and T. F. Baumann, Energy Environ. Sci. **4**, 656 (2011).
[3] F. F. Zhang, J. Tang, N. Shinya, and L. C. Qin, Chem. Phys. Lett. **584**, 124 (2013).
[4] J. C. Rasaiah, S. Garde, and G. Hummer, Annu. Rev. Phys. Chem. **59**, 713 (2008).
[5] M. P. Allen and D. J. Tildesley, *Computer Simulation of Liquids* (Clarendon, Oxford, 1987).
[6] D. J. Adams, Mol. Phys. **29**, 307 (1975).
[7] J. C. Shelley and G. N. Patey, Mol. Phys. **88**, 385 (1996).
[8] L. D. Gelb, K. E. Gubbins, R. Radhakrishnan, and M. Sliwinska-Bartkowiak, Rep. Prog. Phys. **62**, 1573 (1999).
[9] A. Striolo, A. A. Chialvo, P. T. Cummings, and K. E. Gubbins, Langmuir **19**, 8583 (2003).
[10] A. Luzar, D. Bratko, and L. Blum, J. Chem. Phys. **86**, 2955 (1987).
[11] D. Bratko, R. A. Curtis, H. W. Blanch, and J. M. Prausnitz, J. Chem. Phys. **115**, 3873 (2001).
[12] K. Leung, A. Luzar, and D. Bratko, Phys. Rev. Lett. **90**, 065502 (2003).
[13] I. V. Brovchenko, A. Geiger, and D. Paschek, Fluid Phase Equilib. **183**, 331 (2001).
[14] A. Luzar and D. Bratko, J. Phys. Chem. B **109**, 22545 (2005).
[15] D. Bratko and A. Luzar, Langmuir **24**, 1247 (2008).
[16] D. Bratko, B. Jonsson, and H. Wennerstrom, Chem. Phys. Lett. **128**, 449 (1986).

[17]R. K. Kalluri, D. Konatham, and A. Striolo, J. Phys. Chem. C **115**, 13786 (2011).
[18]R. Zangi, M. Hagen, and B. J. Berne, J. Am. Chem. Soc. **129**, 4678 (2007).
[19]R. K. Kalluri, M. M. Biener, M. E. Suss, M. D. Merrill, M. Stadermann, J. G. Santiago, T. F. Baumann, J. Biener, and A. Striolo, Phys. Chem. Chem. Phys. **15**, 2309 (2012).
[20]J. Dzubiella and J. P. Hansen, Mol. Phys. **111**, 3404 (2013).
[21]P. A. Cazade, R. Hartkamp, and B. Coasne, J. Phys. Chem. C **118**, 5061 (2014).
[22]D. Bratko, D. J. Henderson, and L. Blum, Phys. Rev. A **44**, 8235 (1991).
[23]V. Vlachy and A. D. J. Haymet, Aust. J. Chem. **43**, 1961 (1990).
[24]D. Bratko, C. E. Woodward, and A. Luzar, J. Chem. Phys. **95**, 5318 (1991).
[25]T. S. Sorensen and P. Sloth, J. Chem. Soc., Faraday Trans. **88**, 571 (1992).
[26]S. A. Barr and A. Z. Panagiotopoulos, Phys. Rev. E **86**, 016703 (2012).
[27]A. Jusufi, A.-P. Hynninen, M. Haataja, and A. Z. Panagiotopoulos, J. Phys. Chem. B **113**, 6314 (2009).
[28]G. Hummer and D. M. Soumpasis, J. Chem. Phys. **98**, 581 (1993).
[29]R. Kovacs, M. Valisko, and D. Boda, Condens. Matter Phys. **15**, 23803 (2012).
[30]M. Valisko, D. Henderson, and D. Boda, Condens. Matter Phys. **16**, 43601 (2013).
[31]J. C. Shelley and G. N. Patey, J. Chem. Phys. **100**, 8265 (1994).
[32]J. C. Shelley and G. N. Patey, J. Chem. Phys. **102**, 7656 (1995).
[33]M. Lisal, W. R. Smith, and J. Kolafa, J. Phys. Chem. B **109**, 12956 (2005).
[34]F. Moucka, M. Lisal, J. Skvor, J. Jirsak, I. Nezbeda, and W. R. Smith, J. Phys. Chem. B **115**, 7849 (2011).
[35]F. Moucka, M. Lisal, and W. R. Smith, J. Phys. Chem. B **116**, 5468 (2012).
[36]F. Moucka, I. Nezbeda, and W. R. Smith, J. Chem. Phys. **139**, 124505 (2013).
[37]W. Shi and E. J. Maginn, J. Chem. Theory Comput. **3**, 1451 (2007).
[38]K. Lum and A. Luzar, Phys. Rev. E **56**, R6283 (1997).
[39]K. Leung and A. Luzar, J. Chem. Phys. **113**, 5845 (2000).
[40]N. Giovambattista, P. J. Rossky, and P. G. Debenedetti, Annu. Rev. Phys. Chem. **63**, 179 (2012).
[41]N. Giovambattista, P. J. Rossky, and P. G. Debenedetti, Phys. Rev. E **73**, 041604 (2006).
[42]M. Kanduc, E. Schneck, and R. R. Netz, Chem. Phys. Lett. **610**, 375 (2014).
[43]C. D. Daub, D. Bratko, and A. Luzar, J. Phys. Chem. C **115**, 22393 (2011).
[44]D. Vanzo, D. Bratko, and A. Luzar, J. Phys. Chem. B (published online).
[45]R. Zangi and B. J. Berne, J. Phys. Chem. B **110**, 22736 (2006).
[46]H. J. C. Berendsen, J. R. Grigera, and T. P. Straatsma, J. Phys. Chem. **91**, 6269 (1987).
[47]I. S. Joung and T. E. Cheatham, J. Phys. Chem. B **112**, 9020 (2008).
[48]I. S. Joung and T. E. Cheatham, J. Phys. Chem. B **113**, 13279 (2009).
[49]F. Moucka, I. Nezbeda, and W. R. Smith, J. Chem. Phys. **138**, 154102 (2013).
[50]C. Y. Lee, J. A. McCammon, and P. J. Rossky, J. Chem. Phys. **80**, 4448 (1984).
[51]D. Bratko, C. D. Daub, K. Leung, and A. Luzar, J. Am. Chem. Soc. **129**, 2504 (2007).
[52]D. Bratko, C. D. Daub, and A. Luzar, Phys. Chem. Chem. Phys. **10**, 6807 (2008).
[53]D. Vanzo, D. Bratko, and A. Luzar, J. Chem. Phys. **137**, 034707 (2012).
[54]J. Driskill, D. Vanzo, D. Bratko, and A. Luzar, J. Chem. Phys. **141**, 18c517 (2014).
[55]W. L. Jorgensen, J. D. Madura, and C. J. Swenson, J. Am. Chem. Soc. **106**, 6638 (1984).
[56]D. Vanzo, D. Bratko, and A. Luzar, J. Phys. Chem. C **116**, 15467 (2012).
[57]D. Bratko, C. D. Daub, and A. Luzar, Faraday Discuss. **141**, 55 (2009).
[58]D. Frenkel and B. Smit, *Understanding Molecular Simulation, From Algorithms to Applications* (Academic, San Diego, 2002).
[59]M. W. Chase, *Journal of Physical and Chemical Reference Data Monographs ACS* (AIP, 1998).
[60]J. B. Padley, *Thermodynamical Data and Structures of Organic Compounds*, TRC Data Series (Thermodynamic Research Center, College Station, TX, 1994).
[61]D. D. Wagman, J. Phys. Chem. Ref. Data **11**(Supp. 2), 1 (1982).
[62]F. G. Wang and D. P. Landau, Phys. Rev. Lett. **86**, 2050 (2001).
[63]J. Janecek, J. Phys. Chem. B **110**, 6264 (2006).
[64]F. J. Martinez-Ruiz, F. J. Blas, B. Mendiboure, and A. Bravo, J. Chem. Phys. **141**, 184701 (2014).
[65]C. D. Daub, D. Bratko, K. Leung, and A. Luzar, J. Phys. Chem. C **111**, 505 (2007).
[66]I. C. Yeh and M. L. Berkowitz, J. Chem. Phys. **111**, 3155 (1999).
[67]G. J. Gloor, G. Jackson, F. J. Blas, and E. de Miguel, J. Chem. Phys. **123**, 134703 (2005).
[68]V. I. Harismiadis, J. Vorholz, and A. Z. Panagiotopoulos, J. Chem. Phys. **105**, 8469 (1996).
[69]S. Sharma and P. G. Debenedetti, J. Phys. Chem. B **116**, 13282 (2012).
[70]A. Luzar, S. Svetina, and B. Zeks, J. Chem. Phys. **82**, 5146 (1985).
[71]I. Kalcher and J. Dzubiella, Phys. Rev. E **88**, 062312 (2013).
[72]T. Hayashi, A. J. Pertsin, and M. Grunze, J. Chem. Phys. **117**, 6271 (2002).
[73]I. Kalcher, J. C. F. Schulz, and J. Dzubiella, J. Chem. Phys. **133**, 164511 (2011).
[74]F. W. Tavares, D. Bratko, H. W. Blanch, and J. M. Prausnitz, J. Phys. Chem. B **108**, 9228 (2004).
[75]W. R. Smith and B. Triska, J. Chem. Phys. **100**, 3019 (1994).